Article

Geometric and Electronic Structure of the Heme–Peroxo–Copper Complex [(FTPP)Fe–(O)–Cu(TMPA)](ClO)

Diego del Ro, Ritimukta Sarangi, Eduardo E. Chufn, Kenneth D. Karlin, Britt Hedman, Keith O. Hodgson, and Edward I. Solomon

J. Am. Chem. Soc., **2005**, 127 (34), 11969-11978• DOI: 10.1021/ja043374r • Publication Date (Web): 04 August 2005

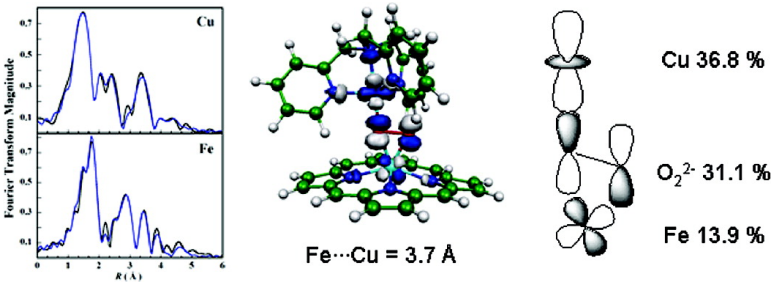

More About This Article

Additional resources and features associated with this article are available within the HTML version:

- Supporting Information
- Links to the 5 articles that cite this article, as of the time of this article download
- Access to high resolution figures
- Links to articles and content related to this article
- Copyright permission to reproduce figures and/or text from this article

View the Full Text HTML

J|A|C|S
ARTICLES
Published on Web 08/04/2005

Geometric and Electronic Structure of the Heme−Peroxo−Copper Complex [(F$_8$TPP)Fe^{III}−(O$_2^{2-}$)−Cu^{II}(TMPA)](ClO$_4$)

Diego del Río,[†] Ritimukta Sarangi,[†] Eduardo E. Chufán,[‡] Kenneth D. Karlin,*[,‡] Britt Hedman,[§] Keith O. Hodgson,[†,§] and Edward I. Solomon*[,†]

Contribution from the Department of Chemistry, Stanford University, Stanford, California 94305, Department of Chemistry, The Johns Hopkins University, 3400 North Charles Street, Baltimore, Maryland 21218, and Stanford Synchrotron Radiation Laboratory, Stanford Linear Accelerator Center, Stanford University, Stanford, California 94309

Received November 2, 2004; E-mail: karlin@jhu.edu; edward.solomon@stanford.edu

Abstract: The geometric and electronic structure of the untethered heme−peroxo−copper model complex [(F$_8$TPP)Fe^{III}−(O$_2^{2-}$)−Cu^{II}(TMPA)](ClO$_4$) (**1**) has been investigated using Cu and Fe K-edge EXAFS spectroscopy and density functional theory calculations in order to describe its geometric and electronic structure. The Fe and Cu K-edge EXAFS data were fit with a Cu···Fe distance of ∼3.72 Å. Spin-unrestricted DFT calculations for the $S_T = 2$ spin state were performed on [(P)Fe^{III}−(O$_2^{2-}$)−Cu^{II}(TMPA)]$^+$ as a model of **1**. The peroxo unit is bound end-on to the copper, and side-on to the high-spin iron, for an overall μ-η^1:η^2 coordination mode. The calculated Cu···Fe distance is ∼0.3 Å longer than that observed experimentally. Reoptimization of [(P)Fe^{III}−(O$_2^{2-}$)−Cu^{II}(TMPA)]$^+$ with a 3.7 Å Cu···Fe constrained distance results in a similar energy and structure that retains the overall μ-η^1:η^2-peroxo coordination mode. The primary bonding interaction between the copper and the peroxide involves electron donation into the half-occupied Cu d_{z^2} orbital from the peroxide π^*_σ orbital. In the case of the Fe^{III}−peroxide η^2 bond, the two major components arise from the donor interactions of the peroxide π^*_σ and π^*_v orbitals with the Fe d_{xz} and d_{xy} orbitals, which give rise to σ and δ bonds, respectively. The π^*_σ interaction with both the half-occupied d_{z^2} orbital on the copper (η^1) and the d_{xz} orbital on the iron (η^2), provides an effective superexchange pathway for strong antiferromagnetic coupling between the metal centers.

1. Introduction

Cytochrome *c* oxidase (C*c*O), a member of the heme−copper oxidase superfamily,[1,2] is a membrane-bound multimetal center enzyme that catalyzes the four-electron, four-proton reduction of dioxygen to water,[3,4] and couples this reaction to a transmembrane proton gradient involving movement of four additional protons across the mitochondrial membrane per O_2 molecule reduced.[5−7] The electrochemical potential gradient

$$O_2 + 4e^- + 8H^+(\text{in}) \rightarrow 2H_2O + 4H^+(\text{out})$$

generated provides the driving force used by adenosine triphosphate (ATP) synthase to form ATP from adenosine diphosphate (ADP) and complete the transduction of energy available from the reduction of O_2 to H_2O. In light of its key biological role, C*c*O has been the subject of numerous biophysical and spectroscopic investigations.

In the functioning form of C*c*O, cytochrome *c* transfers its reducing equivalent, sequentially, to a bis-cysteine-bridged, completely delocalized mixed-valence binuclear copper electron-transfer center (Cu_A). Electrons are thereafter transferred to a low-spin heme *a* and then to the binuclear heme a_3−Cu_B center, where dioxygen reduction takes place (Figure 1). Detailed structural information derives from a number of X-ray diffraction studies on different derivatives.[8−15] Heme a_3 is a high-

[†] Department of Chemistry, Stanford University.
[‡] Department of Chemistry, The Johns Hopkins University.
[§] Stanford Synchrotron Radiation Laboratory.

(1) Calhoun, M. W.; Thomas, J. W.; Gennis, R. B. *Trends Biochem. Sci.* **1994**, *19*, 325−331.
(2) Garcia-Horsman, J. A.; Barquera, B.; Rumbley, J.; Ma, J. X.; Gennis, R. B. *J. Bacteriol.* **1994**, *176*, 5587−5600.
(3) Michel, H.; Behr, J.; Harrenga, A.; Kannt, A. In *Annual Review of Biophysics and Biomolecular Structure*; Stroud, R., Ed.; Annual Reviews Inc.: Palo Alto, CA, 1998; Vol. 27; pp 329−356.
(4) Ferguson-Miller, S.; Babcock, G. T. *Chem. Rev.* **1996**, *96*, 2889−2907.
(5) Ogura, T.; Kitagawa, T. *Biochim. Biophys. Acta−Bioenergetics* **2004**, *1655*, 290−297.
(6) Boulatov, R.; Collman, J. P.; Shiryaeva, I. M.; Sunderland, C. J. *J. Am. Chem. Soc.* **2002**, *124*, 11923−11935.
(7) Wikström, M. *Biochim. Biophys. Acta−Bioenergetics* **2004**, *1655*, 241−247.
(8) Tsukihara, T.; Aoyama, H.; Yamashita, E.; Tomizaki, T.; Yamaguchi, H.; Shinzawaitoh, K.; Nakashima, R.; Yaono, R.; Yoshikawa, S. *Science* **1995**, *269*, 1069−1074.
(9) Iwata, S.; Ostermeier, C.; Ludwig, B.; Michel, H. *Nature* **1995**, *376*, 660−669.
(10) Yoshikawa, S.; Shinzawa-Itoh, K.; Nakashima, R.; Yaono, R.; Yamashita, E.; Inoue, N.; Yao, M.; Fei, M. J.; Libeu, C. P.; Mizushima, T.; Yamaguchi, H.; Tomizaki, T.; Tsukihara, T. *Science* **1998**, *280*, 1723−1729.
(11) Ostermeier, C.; Harrenga, A.; Ermler, U.; Michel, H. *Proc. Natl. Acad. Sci. U.S.A.* **1997**, *94*, 10547−10553.
(12) Harrenga, A.; Michel, H. *J. Biol. Chem.* **1999**, *274*, 33296−33299.
(13) Soulimane, T.; Buse, G.; Bourenkov, G. P.; Bartunik, H. D.; Huber, R.; Than, M. E. *EMBO J.* **2000**, *19*, 1766−1776.
(14) Abramson, J.; Riistama, S.; Larsson, G.; Jasaitis, A.; Svensson-Ek, M.; Laakkonen, L.; Puustinen, A.; Iwata, S.; Wikström, M. *Nat. Struct. Biol.* **2000**, *7*, 910−917.

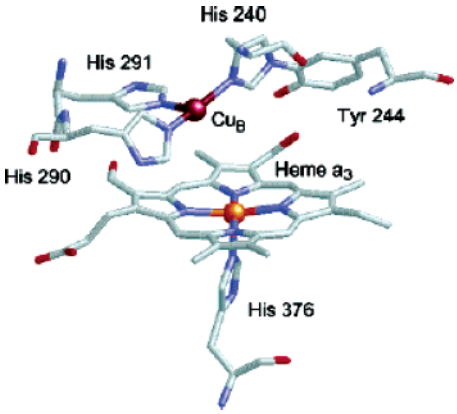

Figure 1. Reduced form of the heme a_3−Cu_B binuclear site of bovine cytochrome *c* oxidase. The $Fe^{II}\cdots Cu^{I}$ distance is 5.19 Å. The figure was generated using the program Rasmol, from Protein Data Bank coordinates (PDB ID 10CR).

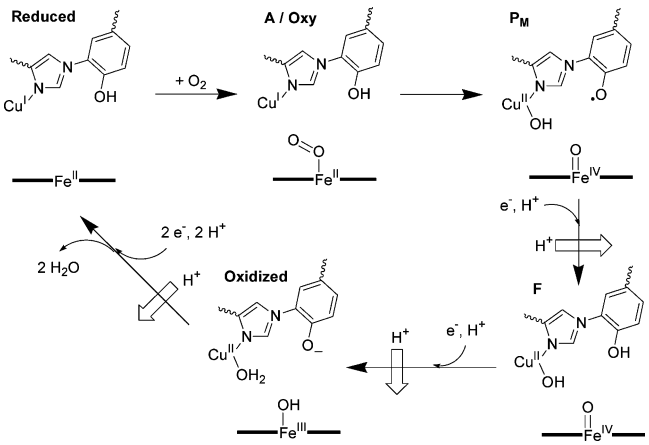

Figure 2. Scheme showing the consensus O_2 reduction mechanism for cytochrome *c* oxidase. See text for details.

spin Fe^{III} center, with a proximal histidine residue. The Cu_B center is located on the distal site of heme a_3. It has three histidine ligands, one of which is covalently linked to a tyrosine, likely a result of a post-translational modification. In the binuclear heme a_3−Cu_B center, the iron−copper separation is in the range of 4.4−5.3 Å, depending on the protein derivative and its oxidation state. This distance would seem to preclude a strong antiferromagnetic interaction, which is consistent with experimental results ($|J| < 1$ cm^{-1});[16] however, some structures suggest the presence of a peroxide bridging ligand between the heme and Cu center,[10] and strong antiferromagnetic coupling has also been reported.[17,18]

Based on extensive kinetic and spectroscopic investigations, there is general agreement on some aspects of O_2 binding and reduction at the heme a_3−Cu_B active site (Figure 2).[19,20] An initial Cu_B−O_2 species is formed,[4] which then transfers O_2 to heme a_3, forming an observable Fe^{III}−superoxo intermediate (**A**). The next detectable intermediate in the reaction cycle is the Fe^{IV}=O species (**P**), and Cu_B^{II}, with either a tyrosinate or a tyrosyl radical, formed after the O−O bond cleavage, depending on the enzyme form used for the O_2 reduction.[20,21] Rapid O−O cleavage seems an attractive mechanistic feature as this bypasses the formation of potentially cytotoxic superoxide or peroxide species. However, the presence of (hydro)peroxide metal-bridged or associated Fe^{III}−OO(H)···Cu_B transients is speculated on the basis of structural, spectroscopic and theoretical considerations.[10,22,23] Reduction leads to intermediate **F**, and the resting oxidized state (**O**) is formed after the fourth e^-/H^+ transfer to generate water.[24] Proton pumping is coupled to the formation of these late intermediates.[7,25]

The study of dioxygen binding and reactivity with heme−copper assemblies is of great importance,[19,26] since the reductive cleavage of O_2 leads to intermediates where the oxygen atoms derived from O_2 are ligated to both the heme and copper centers. The Collman group has carried out extensive electrocatalytic studies of O_2 reduction with heme−copper assemblies and shown that the four-electron, four-proton O_2-reduction process can be achieved by C*c*O model compounds.[26] Also, significant advancements have been made in the generation of O_2 adducts of discrete heme−Cu complexes: (i) Collman et al.[27] and more recently Naruta et *al.*[28] have generated binuclear heme−superoxide−copper moieties. The heme−superoxide moiety is stable even in the presence of the Cu(I) center, which mimics the intermediate **A** in the C*c*O O_2 reduction cycle. (ii) Naruta et al.[29] have determined the crystal structure of a binuclear heme−copper complex, demonstrating a μ-η^1:η^2 Fe^{III}−(O_2^{2-})−Cu^{II} coordination mode. (iii) Karlin et al.[30−38] have characterized a number of heme−O_2−Cu complexes in solution, formed by the reaction of a heme−Fe(II) and a Cu(I) tridentate or tetradentate species with dioxygen. Resonance Raman studies

(15) Svensson-Ek, M.; Abramson, J.; Larsson, G.; Tornroth, S.; Brzezinski, P.; Iwata, S. *J. Mol. Biol.* **2002**, *321*, 329−339.
(16) Cheesman, M. R.; Oganesyan, V. S.; Watmough, N. J.; Butler, C. S.; Thomson, A. J. *J. Am. Chem. Soc.* **2004**, *126*, 4157−4166.
(17) Hagen, W. R. *Biochim. Biophys. Acta* **1982**, *708*, 82−98.
(18) Day, E. D.; Peterson, J.; Sendova, M. S.; Schnoonover, J. R.; Palmer, G. *Biochemistry* **1993**, *32*, 7855−7860.
(19) Kim, E.; Chufan, E. E.; Kamaraj, K.; Karlin, K. D. *Chem. Rev.* **2004**, *104*, 1077−1133.
(20) Babcock, G. T. *Proc. Natl. Acad. Sci. U.S.A.* **1999**, *96*, 12971−12973.
(21) Fabian, M.; Wong, W. W.; Gennis, R. B.; Palmer, G. *Proc. Natl. Acad. Sci. U.S.A.* **1999**, *96*, 13114−13117.
(22) Proshlyakov, D. A.; Pressler, M. A.; Babcock, G. T. *Proc. Natl. Acad. Sci. U.S.A.* **1998**, *95*, 8020−8025.
(23) Blomberg, M. R. A.; Siegbahn, P. E. M.; Wikström, M. *Inorg. Chem.* **2003**, *42*, 5231−5243.
(24) Verkhovsky, M. I.; Jasaitis, A.; Verkhovskaya, M. L.; Morgan, J. E.; Wikström, M. *Nature* **1999**, *400*, 480−483.
(25) Papa, S.; Capitanio, N.; Capitanio, G.; Palese, L. L. *Biochim. Biophys. Acta−Bioenergetics* **2004**, *1658*, 95−105.
(26) Collman, J. P.; Boulatov, R.; Sunderland, C. J.; Fu, L. *Chem. Rev.* **2004**, *104*, 561−588.
(27) Collman, J. P.; Sunderland, C. J.; Berg, K. E.; Vance, M. A.; Solomon, E. I. *J. Am. Chem. Soc.* **2003**, *125*, 6648−6649.
(28) Liu, J. G.; Naruta, Y.; Tani, F. *Angew. Chem., Int. Ed.* **2005**, *44*, 1836−1840.
(29) Chishiro, T.; Shimazaki, Y.; Tani, F.; Tachi, Y.; Naruta, Y.; Karasawa, S.; Hayami, S.; Maeda, Y. *Angew. Chem., Int. Ed.* **2003**, *42*, 2788−2791.
(30) Ghiladi, R. A.; Ju, T. D.; Lee, D. H.; Moënne-Loccoz, P.; Kaderli, S.; Neuhold, Y. M.; Zuberbühler, A. D.; Woods, A. S.; Cotter, R. J.; Karlin, K. D. *J. Am. Chem. Soc.* **1999**, *121*, 9885−9886.
(31) Kopf, M. A.; Karlin, K. D. *Inorg. Chem.* **1999**, *38*, 4922−4923.
(32) Kopf, M. A.; Neuhold, Y. M.; Zuberbühler, A. D.; Karlin, K. D. *Inorg. Chem.* **1999**, *38*, 3093−3102.
(33) Ghiladi, R. A.; Hatwell, K. R.; Karlin, K. D.; Huang, H. W.; Moënne-Loccoz, P.; Krebs, C.; Huynh, B. H.; Marzilli, L. A.; Cotter, R. J.; Kaderli, S.; Zuberbühler, A. D. *J. Am. Chem. Soc.* **2001**, *123*, 6183−6184.
(34) Kim, E.; Helton, M. E.; Wasser, I. M.; Karlin, K. D.; Lu, S.; Huang, H. W.; Moënne-Loccoz, P.; Incarvito, C. D.; Rheingold, A. L.; Honecker, M.; Kaderli, S.; Zuberbühler, A. D. *Proc. Natl. Acad. Sci. U.S.A.* **2003**, *100*, 3623−3628.
(35) Kim, E.; Shearer, J.; Lu, S.; Moënne-Loccoz, P.; Helton, M. E.; Kaderli, S.; Zuberbühler, A. D.; Karlin, K. D. *J. Am. Chem. Soc.* **2004**, *126*, 12716−12717.
(36) Ghiladi, R. A.; Huang, H. W.; Moënne-Loccoz, P.; Stasser, J.; Blackburn, N. J.; Woods, A. S.; Cotter, R. J.; Incarvito, C. D.; Rheingold, A. L.; Karlin, K. D. *J. Biol. Inorg. Chem.* **2005**, *10*, 63−77.
(37) Kim, E.; Kamaraj, K.; Galliker, B.; Rubie, N. D.; Moënne-Loccoz, P.; Kaderli, S.; Zuberbuhler, A. D.; Karlin, K. D. *Inorg. Chem.* **2005**, *44*, 1238−1247.
(38) Kamaraj, K.; Kim, E.; Galliker, B.; Zakharov, L. N.; Rheingold, A. L.; Zuberbühler, A. D.; Karlin, K. D. *J. Am. Chem. Soc.* **2003**, *125*, 6028−6029.

on these complexes reveal that the ν(O−O) can be changed significantly by changing the copper ligand from tetradentate to tridendate (a 40−50 cm^{-1} reduction in ν(O−O)).[34] These peroxo complexes are characterized by strong antiferromagnetic coupling. (iv) Examples of imidazole−phenol covalently linked model complexes that mimic the histidine−tyrosine link of the C*c*O active site have been synthesized.[28,37−39] Investigations on these complexes reveal that a stable heme−peroxo−Cu species is generated in the presence of the phenol which can act as a possible electron−proton source. Interestingly, in the presence of an axial ligand, an Fe−superoxide species is formed.[28]

Despite recent advances, only one of these heme−peroxo−copper complexes has been characterized by X-ray crystallography.[29] Furthermore, no description of the electronic structure of these complexes, or the origin of the strong antiferromagnetic coupling between the Fe^{III} and Cu^{II} centers, has been published. In the present study we have used Cu and Fe K-edge EXAFS (both in solid state and in solution) to probe the structure of the untethered heme−peroxo−copper complex $[(F_8TPP)Fe^{III}-(O_2^{2-})-Cu^{II}(TMPA)](ClO_4)$ (**1**; F_8TPP = tetrakis(2,6-difluorophenyl)porphyrinate; TMPA = tris(2-pyridylmethyl)amine).[33,40] Density functional theory calculations have been employed on $[(P)Fe^{III}-(O_2^{2-})-Cu^{II}(TMPA)]^+$ (P = porphyrinate) as a model for **1**, to describe its geometric and electronic structure. The Cu^{II}−peroxo and Fe^{III}−peroxo bonds have been compared with those obtained for the *trans*-μ-1,2-$[Cu^{II}_2(TMPA)_2(O_2^{2-})]^{2+}$ [41−43] and the side-on peroxo $[(P)Fe^{III}-(O_2^{2-})]^-$ complexes, respectively. The origin of the strong antiferromagnetic coupling ($S_{TOT} = 2$, $-J > 200$ cm^{-1})[33,44] between the high-spin Fe^{III} ($S = {}^5/_2$) and Cu^{II} ($S = {}^1/_2$) has also been defined for the Fe−O_2−Cu center with a μ-η^1:η^2 peroxide bridging mode.

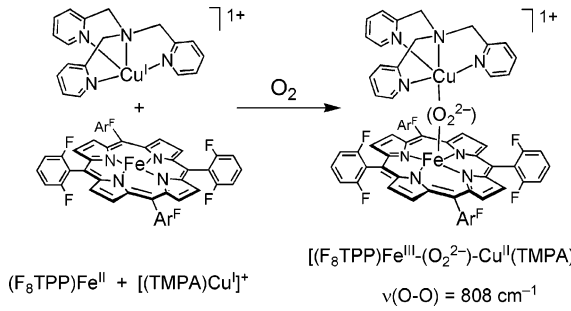

2. Experimental Methods

XAS Sample Preparation. Methods for the preparation of both solid and solution samples of **1** and **L6** (solution only) are given in the Supporting Information.

XAS Data Acquisition and Analysis. The X-ray absorption spectra of $[(F_8TPP)Fe^{III}-O_2-Cu^{II}(TMPA)](ClO_4)$ in both solid and solution forms were measured at the Stanford Synchrotron Radiation Laboratory (SSRL) on the focused 16-pole 2.0-T wiggler beam line 9-3. A Si(220) double-crystal monochromator was used for energy selection. A Rh-coated harmonic rejection mirror and a cylindrical Rh-coated bent focusing mirror were used for beam line 9-3. The solid sample was finely ground with BN into a homogeneous mixture and pressed into a 1-mm aluminum spacer between X-ray-transparent Kapton tape at dry ice temperature and under an inert N_2 atmosphere. The solution samples (~180 μL) were transferred into 2-mm delrin XAS cells with 37-μm Kapton tape windows at −40 °C, immediately frozen thereafter, and stored under liquid N_2. During data collection, the samples were maintained at a constant temperature of 10 K using an Oxford Instruments CF 1208 liquid helium cryostat. Transmission mode was used to measure data to $k = 14$ $Å^{-1}$ at the Cu K-edge and to $k = 17$ $Å^{-1}$ at the Fe K-edge for the solid samples, and fluorescence mode was used to collect data to $k = 13.4$ $Å^{-1}$ at the Cu K-edge and to $k = 16$ $Å^{-1}$ at the Fe K-edge by using a Canberra Ge 30-element array detector. Internal energy calibration was accomplished by simultaneous measurement of the absorption of the corresponding metal foil placed between two ionization chambers situated after the sample. The first inflection point of the foil spectrum was assigned to 8980.3 eV for Cu and 7111.2 eV for Fe. Data represented here are a 4-scan (Cu K-edge) and a 3-scan (Fe K-edge) average spectrum for the solid sample and an 8-scan (Cu K-edge) and a 16-scan (Fe K-edge) average spectrum for the solution sample. The data were processed by fitting a second-order polynomial to the pre-edge region and subtracting this from the entire spectrum as background. A three-region spline of orders 2, 3, and 3 was used to model the smoothly decaying post-edge region. The data were normalized by subtracting the cubic spline and by assigning the edge jump to 1.0 at 9000 eV (Cu K-edge) and 7130 eV (Fe K-edge) using the SPLINE program in the XFIT suite of programs.[45] Theoretical EXAFS signals $\chi(k)$ were calculated using FEFF (version 7.0)[46,47] and fit to the data using EXAFSPAK.[48] The oxo complex $[(F_8TPP)Fe^{III}-O-Cu^{II}(TMPA)]^+$ was chosen as the starting model to generate phase and amplitude parameters. Several structures with the Fe atom 0.4−0.6 Å above the plane were chosen to obtain theoretical parameters. The fit was not particularly sensitive to different input parameters generated from various structures with different Fe−heme plane distances, and the fit refined to the same parameter space in each case. The structural parameters varied during the fitting process were the bond distance R and the bond variance σ^2, which is related to the Debye−Waller factor resulting from thermal motion and static disorder of the absorbing and scattering atoms. The non-structural parameter E_0 (the energy at which $k = 0$) was also allowed to vary but was restricted to a common value for every component in a given fit. Coordination numbers were systematically varied in the course of the fit but were fixed within a given fit.

Computational Details. Density functional theory (DFT) calculations of the model complex $[(P)Fe^{III}-(O_2^{2-})-Cu^{II}(TMPA)]^+$, as well as *trans*-$\mu$-1,2-$[Cu^{II}_2(TMPA)_2(O_2^{2-})]^{2+}$ and the side-on $[(P)Fe^{III}-(O_2^{2-})]^-$ peroxo complexes, were performed using the Gaussian98−03 package of programs.[49] All calculations were spin-unrestricted, allowing for an accurate description of the electronic structure of the antiferromagnetically coupled system. Preliminary optimizations of the model complex were performed using the 6-311G basis set for Fe, Cu, and O atoms, 6-31G* for N, and STO-3G for C and H, and different functionals: BP86,[50,51] B3LYP,[52−54] PW91PW91,[55,56] BLYP,[50,52,53] and B3PW91.[54−56] B3LYP predicts an intermediate spin for Fe^{III}, incon-

(39) Liu, J. G.; Naruta, Y.; Tani, F.; Chishiro, T.; Tachi, Y. *Chem. Commun.* **2004**, 120−121.
(40) Chufan, E. E.; Karlin, K. D. *J. Am. Chem. Soc.* **2003**, *125*, 16160−16161.
(41) Baldwin, M. J.; Ross, P. K.; Pate, J. E.; Tyeklár, Z.; Karlin, K. D.; Solomon, E. I. *J. Am. Chem. Soc.* **1991**, *113*, 8671−8679.
(42) Tyeklár, Z.; Jacobson, R. R.; Wei, N.; Murthy, N. N.; Zubieta, J.; Karlin, K. D. *J. Am. Chem. Soc.* **1993**, *115*, 2677−2689.
(43) Chen, P.; Fujisawa, K.; Helton, M. E.; Karlin, K. D.; Solomon, E. I. *J. Am. Chem. Soc.* **2003**, *125*, 6394−6408.
(44) Karlin, K. D., and co-workers, unpublished results.
(45) Ellis, P. J.; Freeman, H. C. *J. Synchrotron. Radiat.* **1995**, *2*, 190−195.
(46) Mustre de Leon, J.; Rehr, J. J.; Zabinsky, S. I.; Albers, R. C. *Phys. Rev. B.* **1991**, *44*, 4146−4156.
(47) Rehr, J. J.; Mustre de Leon, J.; Zabinsky, S. I.; Albers, R. C. *J. Am. Chem. Soc.* **1991**, *113*, 5135−5140.
(48) George, G. N. *EXAFSPAK*; Stanford Synchrotron Radiation Laboratory, Stanford Linear Accelerator Center, Stanford University: Stanford, CA, 2000.
(49) Frisch, M. J.; et al. *Gaussian 03*, revision C.02; Gaussian Inc.: Wallingford, CT, 2004.
(50) Becke, A. D. *Phys. Rev. A* **1988**, *38*, 3098−3100.
(51) Perdew, J. P. *Phys. Rev. B* **1986**, *33*, 8822−8824.
(52) Lee, C. T.; Yang, W. T.; Parr, R. G. *Phys. Rev. B* **1988**, *37*, 785−789.
(53) Miehlich, B.; Savin, A.; Stoll, H.; Preuss, H. *Chem. Phys. Lett.* **1989**, *157*, 200−206.
(54) Becke, A. D. *J. Chem. Phys.* **1993**, *98*, 5648−5652.

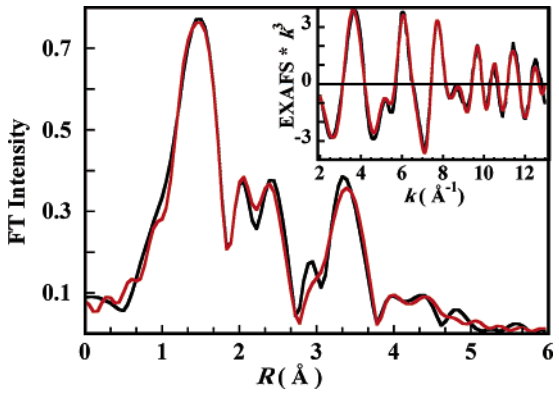

Figure 3. Cu K-edge EXAFS data and non-phase-shift-corrected Fourier transform (inset) of **1** in the solid phase. Phase shift in the first shell is ~0.4 Å. Data (black line); fit (red line).

sistent with experiment, while all other functionals reproduce the antiferromagnetic coupling between high-spin Fe^{III} and Cu^{II}, as observed experimentally. On the basis of this and our previous experience, the BP86 functional was chosen for this study. The structure of the model complex $[(P)Fe^{III}-(O_2^{2-})-Cu^{II}(TMPA)]^+$ was then fully optimized using the 6-311G* basis set for Fe, Cu, and O atoms, 6-31G* for N, and 6-31G for C and H. This structure was characterized as an energy minimum (NImag = 0) by diagonalization of the analytically computed Hessian. Figures and orbitals were drawn using Molekel.[57] The molecular orbital analysis was done using AOMIX.[58,59]

3. Results and Analysis

3.1. Cu EXAFS. The k^3-weighted Cu K-edge EXAFS data and their Fourier transforms (FT) are presented in Figures 3 and S1 (Supporting Information). Figure 3 shows the Cu EXAFS and FT of **1** in the solid form measured in transmission mode. The EXAFS fit parameters are given in Table 1. The Cu K-edge first-shell EXAFS was fit with one Cu−O/N contribution at 1.87 Å and four Cu−N/O at 2.04 Å.[60] The FT shows intense peaks in the $R = 2-3$ Å range, indicating a strong contribution from the tris(2-pyridylmethyl)amine (TMPA) ligand. This second-shell contribution ($R = 2-3$ Å) was fit using single scattering (SS) and multiple scattering (MS) contributions from the TMPA ligand pyridine rings (Table 1). The intense peak at $R = 3-4$ Å was fit with a Cu···Fe SS contribution at 3.68 Å and its corresponding MS pathway at 3.83 Å when both distances and the σ^2 value were allowed to float independently for these paths; however, linking the σ^2 value for these paths resulted in a fit with a Cu···Fe distance of 3.71 Å. The intensity between $R = 4$ Å and $R = 5$ Å was fit using SS and MS contributions from the pyridine carbon atoms (C3, C4, and C5).

Since the UV−visible, resonance Raman, NMR, and Mössbauer spectroscopies[33] were performed in solution, we also measured the XAS spectra of **1** in solution to account for any structural change which could accompany precipitation or crystallization. Figure S1 shows the EXAFS and FT (and the corresponding fits) of **1** in solution collected in fluorescence mode. The data for the solution look very similar to those of the solid (Figure S2, Supporting Information), indicating that there is no significant change in the Fe−O_2−Cu binding mode. The best fit parameters are given in Table S1 (Supporting Information). The solution spectrum, as expected, is noisier than that of the solid. There is a larger disorder in the bond distances in the solution form, resulting in the observed increase in the σ^2 value of individual paths in the fit. This can be observed when the solution data are fit with the same number of SS and MS components as solid data. The best fit parameters given in table S1 correspond to the best fit situation, as estimated by visual inspection of the fit and the fit index. The Cu···Fe SS contribution is linked to the corresponding MS path and is fit at 3.72 Å (compared to 3.71 Å for the EXAFS spectrum of the solid, obtained when the SS and MS contributions are linked); since the error in Cu···Fe bond distance determination is ±0.05 Å, the fits to the solution and solid data give equivalent results.[63]

3.2. Fe EXAFS. The k^3-weighted Fe K-edge EXAFS data and their Fourier transforms (FT) are presented in Figures 4 and S3 (Supporting Information). Figure 4 shows the Fe EXAFS and FT of **1** in the solid form measured in transmission mode. The EXAFS between $k = 2$ and ~10 $Å^{-1}$ is strongly dominated by single and multiple scattering contributions from the symmetrical heme moiety around the Fe(III) center interfering with signal deriving from the Fe···Cu interaction. However, the EXAFS data from $k = \sim10$ to ~17 $Å^{-1}$ are dominated by the Fe···Cu SS and MS contributions, since a metal−metal EXAFS amplitude envelope peaks at high k. Thus, it is important to obtain data to high k to confidently determine the metal−metal vector in systems which also contain heme backscattering ligands.[64] The rich intensity pattern in the EXAFS data is reflected in the FT, which consists of high-intensity peaks to $R = \sim4$ Å. The first backscattering shell was fit using one Fe−O/N contribution at 1.94 Å and four Fe−N/O contributions at 2.1 Å.[65] Note that while a sixth Fe−O contribution might be expected from the second oxygen in the μ-η^2-(O_2^{2-}) bond to Fe^{III} (vide infra), its inclusion resulted in a worse fit. The second shell was fit using the porphyrin pyrrole β carbon SS and MS contributions, and the SS contribution from the meso carbons. To test the reliability in the Fe···Cu distance determination, theoretical phase and amplitude parameters were calculated for seven structural models, varying the Fe···Cu interaction from 3.4 to 4.0 Å (in 0.1 Å increments). The best fit to the data was consistently obtained with an Fe···Cu distance of 3.72 Å for all initial paths between 3.5 and 3.9 Å, whereas models based on 3.4 and 4.0 Å distances did not fit the data. The MS Fe−O−Cu path refined to 3.88 Å. The intensity in the $R = 4-5$ Å

(55) Perdew, J. P.; Burke, K.; Wang, Y. *Phys. Rev. B (Condensed Matter)* **1996**, *54*, 16533−16539.
(56) Burke, K.; Perdew, J. P.; Wang, H. X. *Electronic Density Functional Theory: Recent Progress and New Directions*; Plenum: New York, 1998.
(57) Portmann, S.; Luthi, H. P. *Chimia* **2000**, *54*, 766−770.
(58) Gorelsky, S. I. *AOMix program*, Revision 6.05; Stanford University: Stanford, CA, 2004 (http://www.sg-chem.net/).
(59) Gorelsky, S. I.; Lever, A. B. P. *J. Organomet. Chem.* **2001**, *635*, 187−196.
(60) The phase and amplitude envelope of an EXAFS single scattering (SS) contribution is nearly identical and indistinguishable by the fitting routines for scatterers with atomic number Z and $Z \pm 1$ located at the same distance from the absorber. Fe−O/N refers to a SS contribution from either O or N; however, the theoretical phase and amplitude parameters were calculated for an Fe−O path.
(61) Penner-Hahn, J. E. *Coord. Chem. Rev.* **1999**, *192*, 1101−1123.
(62) Teo, B. K. *EXAFS: Basic Principles and Data Analysis*; Springer-Verlag: Berlin, 1986.
(63) The Cu···Fe SS and MS paths are strongly correlated. The disorder in the MS path in solution is larger than that in the solid. This, in addition to the higher noise level in the solution data, increases the error bar on the metal−metal distance determination.
(64) Zhang, H. H.; Filipponi, A.; Di Cicco, A.; Lee, S. C.; Scott, M. J.; Holm, R. H.; Hedman, B.; Hodgson, K. O. *Inorg. Chem.* **1996**, *35*, 4819−4828.
(65) For speed of convergence, the structure of the model complex $[(P)Fe^{III}-O_2-Cu^{II}(TMPA)]^+$ with the Fe···Cu constrained at different values between 3.6 and 4.15 Å was calculated using the Jaguar program at the BP86 level of theory, resulting in an energy difference between the fully optimized structure and that with an Fe···Cu distance constrained at 3.7 Å of 7.1 kcal/mol. Details of these calculations are given in Supporting Information.

Table 1. EXAFS Least-Squares Fitting Results for $[(F_8TPP)Fe^{III}-(O_2^{2-})-Cu^{II}(TMPA)](ClO_4)$ in Solid Form[61,62]

Fe					Cu				
coord./path	R (Å)[a]	σ^2 (Å^2)[b]	ΔE_0 (eV)	F[c]	coord./path	R (Å)[a]	σ^2 (Å^2)[b]	ΔE_0 (eV)	F[c]
1 Fe−O/N	1.94	249			1 Cu−O/N	1.87	270		
4 Fe−N/O	2.10	278			4 Cu−N/O	2.04	497		
8 Fe−C	3.11	499			8 Cu−C	2.89	1037		
4 Fe−C	3.41	253			16 Cu−C−N	3.18	1173	−8.78	0.06
1 Fe−Cu	3.72	318	−2.06	0.17	1 Cu−Fe	3.68	258		
2 Fe−O−Cu	3.82	727			2 Cu−O−Fe	3.83	957		
8 Fe−C	3.93	259			4 Cu−C−N	4.80	230		
16 Fe−C−N	4.17	687							
4 Fe−C	4.85	690							
8 Fe−C−C[d]	4.94	690							

[a] The estimated standard deviations for the distances are in the order of ±0.02 Å (for the first shell). [b] The σ^2 values are multiplied by 10^5. [c] Error is given by $\sum[(\chi_{obsd} - \chi_{calcd})^2k^6]/\sum[(\chi_{obsd})^2k^6]$. [d] The σ^2 factor of the multiple scattering path is linked to that of the corresponding single scattering path. The estimated errors in the ΔE_o values are ±0.29 eV for Fe and ±0.19 eV for Cu (as estimated by EXAFSPAK). The estimated errors in the Debye−Waller factors are between 5 and 12%.

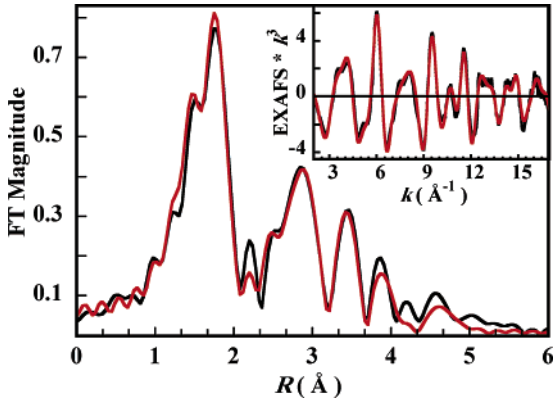

Figure 4. Fe K-edge EXAFS data and non-phase-shift-corrected Fourier transform (inset) of **1** in the solid phase. Phase shift in the first shell is ~0.4 Å. Data (black line); fit (red line).

range was fit with SS and MS components from the porphyrin pyrrole α and γ carbon atoms.

Figure S3 shows the Fe EXAFS and FT (and the corresponding fits) of **1** in solution measured as fluorescence data. The solution EXAFS spectrum is noisier at high k compared to the spectrum of the solid (Figure S4, Supporting Information), and there are small differences in the EXAFS peak intensities for the data of the two forms which could not be subtracted through alternative splining approaches. Overall, the two data sets overlap reasonably well (Figure S4), indicating that there is no major change in the Fe−O_2−Cu core or in the molecule. The first shell of the FT was fit using one Fe−O/N contribution at 1.93 Å and five Fe−N/O contributions at 2.09 Å. The fit to the solution spectrum can accommodate a fifth Fe−O/N ligand. The Cu···Fe contribution is fit at 3.75 Å (compared to 3.72 Å for the solid EXAFS spectrum). Thus, both Fe and Cu EXAFS data indicate a Cu−Fe bond distance of 3.72 ± 0.05 Å.

3.3. DFT Calculations. 3.3.1. Geometric Structure. Spin-unrestricted DFT calculations were performed on the complex $[(P)Fe^{III}-(O_2^{2-})-Cu^{II}(TMPA)]^+$, as a model for **1**, using the BP86 functional. Figure 5A shows two orientations of the final optimized structure. Selected bond distances and angles are compared to experimental data in Table 2. The most relevant feature of the optimized structure is the overall μ:η^2-η^1 peroxo coordination, which is very similar to that in the crystallographically characterized tethered complex $[(TMP)Fe^{III}-(O_2^{2-})-Cu^{II}(5MeTPA)]^+$ (**2**) (TMP-5MeTMPA = 6-{[bis-(5-methylpyridin-2-ylmethyl)amino]methyl}-*N*-{2-[tris(2,4,6-trimethylphenyl)porphyrinate]phenyl}nicotinamide) of Naruta et al.[29] The peroxo unit is bound end-on to the Cu^{II} center (Cu−O2 = 1.959 Å), while the high-spin Fe^{III} center, situated 0.534 Å above the plane formed by the nitrogen atoms of the porphyrin ring, has the peroxide bound in a side-on (η^2) structure, with Fe−O distances of 1.880 (O3) and 2.072 Å (O2). The O−O distance is 1.423 Å, and the distance from the center of the O−O bond to the Fe is 1.846 Å. In general, these values are in good

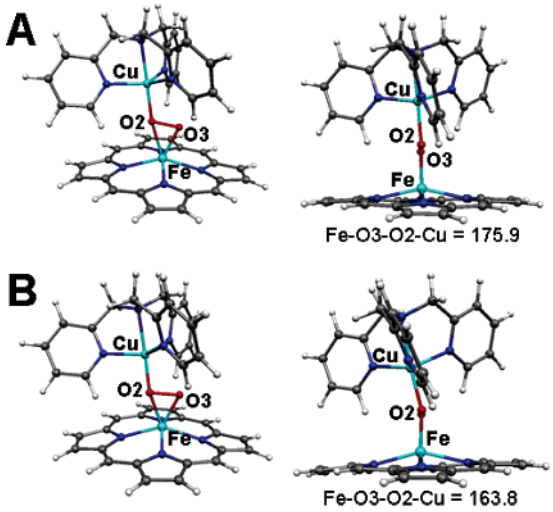

Figure 5. Front and side views of the fully optimized (A) and Fe···Cu = 3.7 Å constrained (B) structures of the model complex $[(P)Fe^{III}-(O_2^{2-})-Cu^{II}(TMPA)]^+$.

Table 2. Selected Bond Distances (Å) and Angles (°) of the Fully Optimized and the Constrained Structures (Fe···Cu = 3.7 Å) of the Model Complex $[(P)Fe^{III}-(O_2^{2-})-Cu^{II}(TMPA)]^+$

	DFT fully optimized structure	DFT structure with constrained Fe···Cu = 3.7 Å	EXAFS Cu (Fe) edge	crystal structure of **2**
Fe−Cu	4.006	3.700[b]	3.68 (3.71)	3.916
O2−O3	1.423	1.446		1.460(6)
Cu−O2	1.959	1.854	1.87	1.915(5)
Fe−O2	2.072	1.900		2.031(4)
Fe−O3	1.880	1.891	(1.94)	1.890(6)
Fe−D1	1.846	1.752		
Fe−D2	0.534	0.585		0.534
Cu−O−Fe	170.1	160.6	149.9[c]	166.3(3)
Cu−O2−O3	109.0	101.0		103.0(4)
Fe−O3−O2−Cu	−175.9	−163.8		178.0

[a] Structural data from Cu and Fe K-edge EXAFS of **1** and from X-ray structure of complex **2** are included for comparison. [b] Frozen. [c] Calculated using MS 2(Cu1−O2−Fe1) = 3.83° (3.82°) .

agreement with the structural parameters obtained for **1** from both Cu and Fe K-edge EXAFS (vide infra) and those obtained by X-ray diffraction on **2**. However, while the calculated Fe···Cu distance (4.006 Å) is in good agreement with that observed in the tethered complex **2** (i.e., with a chemically linked Cu−ligand moiety),[29] it is ∼0.3 Å longer than that observed for **1** (3.7 Å in both the solid state and acetonitrile solution).

To obtain further insight into this difference, a geometry optimization of $[(P)Fe^{III}-(O_2^{2-})-Cu^{II}(TMPA)]^+$ was performed with the Fe···Cu constrained at 3.7 Å.[65] Selected bond distances and angles for the fully optimized and the constrained partially optimized structure are presented in Table 2. Figure 5B shows two different views of the optimized structure with the 3.7 Å Fe···Cu constraint. The constrained optimized structure retains the overall μ:η^2-η^1 peroxo coordination to the Fe and Cu, respectively. However, due to the shortening of the Fe···Cu bond, the Cu−O and Fe−O distances become shorter (Table 2). Although the Fe−O3 distance increases slightly from 1.880 to 1.891 Å, the Fe−O2 distance decreases from 2.072 to 1.900 Å, resulting in an overall decrease in the distance between the Fe and the center of the O−O bond (Fe−D1 = 1.846 Å, Table 2). Additionally, the O−O bond becomes slightly longer and the Fe is pulled out of the porphyrin plane to 0.585 Å, from 0.534 Å in the fully optimized structure. The major structural change is the bending of the Fe−O2−Cu and the Fe−O3−O2−Cu angles, from 170.1° to 160.6° and from 175.9° to 163.8°, respectively, resulting in the bent butterfly constrained structure shown in Figure 5B. Also note that the constrained 3.7 Å Fe···Cu $[(P)Fe^{III}-(O_2^{2-})-Cu^{II}(TMPA)]^+$ structure has a more symmetric η^2-O_2^{2-} coordination to the iron (Fe−O2 = 1.900 Å and Fe−O3 = 1.890 Å vs Fe−O2 = 2.072 Å and Fe−O3 = 1.880 Å for the fully optimized structure). However, the energy difference between the two structures is very small (3.5 kcal/mol). The limited difference between the EXAFS experimental results and the computed complete geometry optimization can be associated with some structural differences between **1** and the calculated model complex. In particular, the effects of the fluorinated phenyl substituents on the porphyrin and the counterion are not included in these calculations.

3.3.2. Electronic Structure. In this $S_T = 2$ spin-unrestricted description of the $[(P)Fe^{III}-(O_2^{2-})-Cu^{II}(TMPA)]^+$ model complex, the high-spin Fe^{III} and the Cu^{II} centers are antiferromagnetically coupled. One unoccupied α-spin is localized on the Cu center, while five unoccupied β-spins are localized on the iron. The calculated antiferromagnetic exchange splitting between the $S_T = 2$ and $S_T = 3$ states, $^5/_2 J = -4950$ cm^{-1}, is in general agreement with experiment (vide supra).[66] Selected molecular orbital (MO) contour plots and an energy level diagram for the fully optimized structure are given in Figures 6 and 7, while those corresponding to the optimized structure with a 3.7 Å constrained Fe···Cu distance are given as Supporting Information. Table 3 shows the composition and assignment of orbitals of particular interest.

3.3.2-A. Nature of the Cu−Peroxide Bond. A general bonding description of the end-on bonding of peroxide to the Cu^{II} center has been obtained using unrestricted DFT calculations. The antibonding molecular orbital corresponding to the Cu^{II}−peroxide interaction on $[(P)Fe^{III}-(O_2^{2-})-Cu^{II}(TMPA)]^+$,

(66) Coupling constants calculated with pure DFT methods are normally 2−3 times larger than the experimental values.

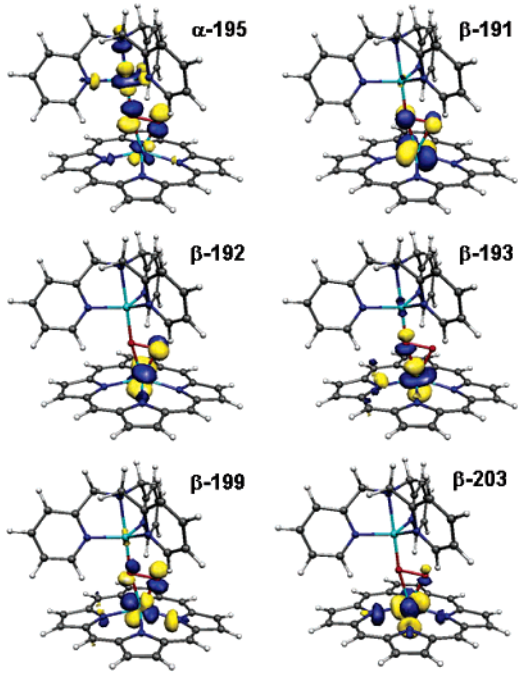

Figure 6. Molecular orbital contour plots for the fully optimized antiferromagnetically coupled $S_T = 2$ model complex $[(P)Fe^{III}-(O_2^{2-})-Cu^{II}(TMPA)]^+$. The unoccupied α MO with predominant Cu character, and the five unoccupied β MOs with predominant Fe 3d character, are shown.

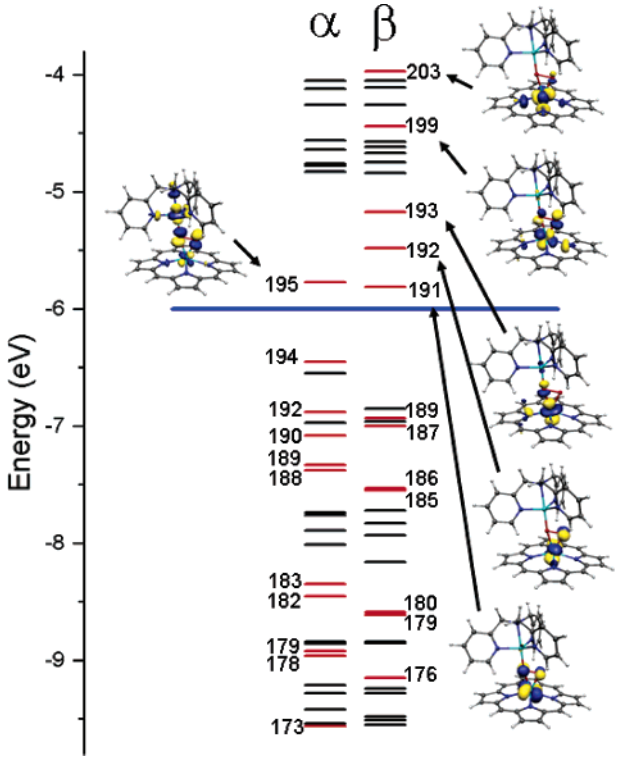

Figure 7. Energy level diagram, and selected MO contour plots, for the fully optimized antiferromagnetically coupled $S_T = 2$ model complex $[(P)Fe^{III}-(O_2^{2-})-Cu^{II}(TMPA)]^+$. MOs with significant contribution from Fe^{III}, Cu^{II}, and O_2^{2-} are presented in red.

the spin-up LUMO α-195 (Figure 6), is composed primarily of the Cu d_{z^2} (36.1%) and the in-plane peroxide π^*_σ (33.3%) orbitals.[67] This orbital also contains some contribution from the axial nitrogen of the TMPA ligand and from the Fe d_{xz} (11.2%),

Table 3. MO Composition, Energies, and Assignment for Selected Orbitals of the Fully Optimized and Constrained $[(P)Fe^{III}-(O_2^{2-})-Cu^{II}(TMPA)]^+$ Model Complex[a]

	$[(P)Fe^{III}-O_2-Cu^{II}(TMPA)]^+$ fully optimized structure			$[(P)Fe^{III}-(O_2^{2-})-Cu^{II}(TMPA)]^+$ constrained structure (Fe···Cu = 3.7 Å)			$[(P)Fe^{III}(O_2^{2-})]^-$ fully optimized structure	
	α 195	β 191	β 199	α 195	β 191	α 199	β 102	β 107
energy (eV)	−5.77	−5.81	−4.44	−5.75	−5.84	−4.40	0.53	2.04
Fe d_{xz}	11.2	0.0	47.9	8.2	0.0	48.2	0.0	59.6
Fe d_{xy}	0.0	69.6	0.0	0.0	63.9	0.0	50.1	0.0
total Cu	36.7	0.9	2.5	36.8	1.9	1.37	- - -	- - -
O2 p_y	0.0	8.5	0.0	0.4	8.6	0.0	24.0	0.0
O2 p_z	17.8	0.0	4.0	15.7	0.0	5.6	0.0	16.3
O3 p_y	0.0	6.1	0.0	0.1	9.1	0.0	24.0	0.0
O3 p_z	14.6	0.0	11.8	12.2	0.0	12.2	0.0	16.3
		$d_{xy} + \pi^*_v$ δ bond	$d_{xz} + \pi^*_\sigma$ σ bond		$d_{xy} + \pi^*_v$ δ bond	$d_{xz} + \pi^*_\sigma$ σ bond	$d_{xy} + \pi^*_v$ δ bond	$d_{xz} + \pi^*_\sigma$ σ bond

[a] MO composition and assignment of selected orbitals of the $[(P)Fe^{III}(O_2^{2-})]^-$ complex are included for comparison. A more complete version of this table can be found in Supporting Information.

making it responsible for the observed strong antiferromagnetic interaction (see below).[68] The Cu^{II}−peroxide bonding in $[(P)Fe^{III}-(O_2^{2-})-Cu^{II}(TMPA)]^+$ is very similar to that described in detail for the $[Cu^{II}_2(TMPA)_2(O_2^{2-})]^{2+}$ complex, in which the Cu^{II} centers are in an idealized trigonal bypyramidal environment bridged by a peroxide in a *trans*-μ-1,2 geometry.[41−43] In this complex the primary bonding interaction involves electron donation into the half-occupied Cu d_{z^2} orbital from the π^*_σ orbital of the peroxide. For $[Cu^{II}_2(TMPA)_2(O_2^{2-})]^{2+}$ the amounts of Cu(1) d_{z^2} (37.7%) and peroxide π^*_σ (36.6%) of the unoccupied spin-up MO are slightly higher than those for $[(P)Fe^{III}-(O_2^{2-})-Cu^{II}(TMPA)]^+$.[69,70] Also, the contribution of the Fe d_{xz} orbital in the spin-up LUMO in $[(P)Fe^{III}-(O_2^{2-})-Cu^{II}(TMPA)]^+$ is somewhat larger (11.2%) than that of the Cu(2) d_{z^2} orbital in $[Cu^{II}_2(TMPA)_2(O_2^{2-})]^{2+}$ (9.5%). This results in a stronger Cu−peroxo bond in the binuclear $[Cu^{II}_2(TMPA)_2(O_2^{2-})]^{2+}$ than in the heteronuclear $[(P)Fe^{III}-(O_2^{2-})-Cu^{II}(TMPA)]^+$ complex, as reflected in their calculated Cu−O distances, 1.92 and 1.96 Å, respectively.

3.3.2-B. Nature of the η^2-Peroxide−Fe^{III} Bond. (i) $[(P)Fe^{III}-(O_2^{2-})]^-$. To better understand the nature of the Fe^{III}−peroxo bond in the model complex $[(P)Fe^{III}-(O_2^{2-})-Cu^{II}(TMPA)]^+$, geometry optimization was also performed on a monomeric side-on peroxo Fe^{III}(porphyrin) complex, $[(P)Fe^{III}-(O_2^{2-})]^-$, to generate a comparable bonding description. Anionic heme−Fe^{III}−peroxo complexes can be formed by the reaction of Fe^{II} with superoxide[71,72] or chemical oxidation.[40] DFT calculations were performed on the model complex $[(P)Fe^{III}-(O_2^{2-})]^-$ under C_{2v} symmetry using the same level of theory employed above for $[(P)Fe^{III}-(O_2^{2-})-Cu^{II}(TMPA)]^+$.[73] A figure of the fully optimized structure, a table with selected bond distances and angles, and a complete MO diagram are given in Supporting Information. Mixing coefficients for selected MOs are given in Table 3 for comparison to the $[(P)Fe^{III}-(O_2^{2-})-Cu^{II}(TMPA)]^+$ complex.

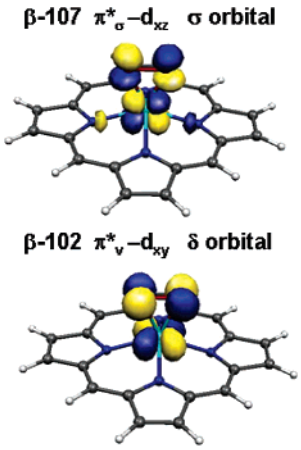

Figure 8. Selected spin-down unoccupied MO contour plots for the model complex $[(P)Fe^{III}-(O_2^{2-})]^-$, showing the σ and δ components of the Fe^{III}−peroxide bond.

For this bonding description, the porphyrin is again defined as the *xy* plane, with the *x* axis along the O−O vector. The two major components of the Fe^{III}−peroxide bond arise from the mixing of the π^*_σ and π^*_v orbitals of the peroxide with the Fe d_{xz} and d_{xy} orbitals which give rise to σ and δ interactions, respectively.[74,75] Figure 8 shows the corresponding unoccupied spin-down MOs, β-102 and β-107. The β-102 MO (δ bond) consists of 50% Fe d_{xy} character and 48% of π^*_v, while the β-107 MO (σ bond) consists of 60% Fe d_{xz} character and 33% of π^*_σ. A small amount of mixing also occurs between the d_{yz} (81%) and π_v (<5%) (β-103, π bond) and d_{z^2} (81%) and π_σ (6%) (β-104, σ bond).[76] Despite the higher mixing coefficient of β-102, the σ bond in β-107 is stronger than the δ bond, as reflected by the larger splitting of its corresponding bonding

(67) The highest occupied orbitals of the peroxide are the two degenerate π^* orbitals, which split in energy upon the interaction with the metal centers. The peroxide π^*_σ is in the Fe−O_2−Cu plane, while the π^*_v is perpendicular to the Fe−O_2−Cu plane.
(68) For this bonding description, the porphyrin is defined as the *xy* plane, with the *z* axis perpendicular to this plane and the *x* axis along the O−O vector.
(69) The $[Cu_2(TMPA)_2(O_2)]^{2+}$ complex has already been described.[41−43] In this study, geometry optimization of $[Cu_2(TMPA)_2(O_2)]^{2+}$ was performed at the same level of theory as $[(P)Fe^{III}-O_2-Cu^{II}(TMPA)]^+$ to provide a better basis for comparison. Details are given in Supporting Information.
(70) In the broken symmetry description ($S = 0$), each spin-up orbital is energetically degenerate with a spin-down electron on the opposite site of the molecule. Such spin-up and spin-down electrons are images of one another under inversion.
(71) Burstyn, J. N.; Roe, J. A.; Miksztal, A. R.; Shaevitz, B. A.; Lang, G.; Valentine, J. S. *J. Am. Chem. Soc.* **1988**, *110*, 1382−1388.
(72) Selke, M.; Sisemore, M. F.; Valentine, J. S. *J. Am. Chem. Soc.* **1996**, *118*, 2008−2012.
(73) The $[(P)Fe^{III}-O_2]^-$ model complex was also optimized using a larger basis set containing diffuse functions. In particular, the basis set 6-311+G* was used for Fe and O, and the basis set 6-31+G* was used for N, C, and H. The results are very similar to those presented here.
(74) Vanatta, R. B.; Strouse, C. E.; Hanson, L. K.; Valentine, J. S. *J. Am. Chem. Soc.* **1987**, *109*, 1425−1434.
(75) Cramer, C. J.; Tolman, W. B.; Theopold, K. H.; Rheingold, A. L. *Proc. Natl. Acad. Sci. U.S.A.* **2003**, *100*, 3635−3640.
(76) Neese, F.; Solomon, E. I. *J. Am. Chem. Soc.* **1998**, *120*, 12829−12848.

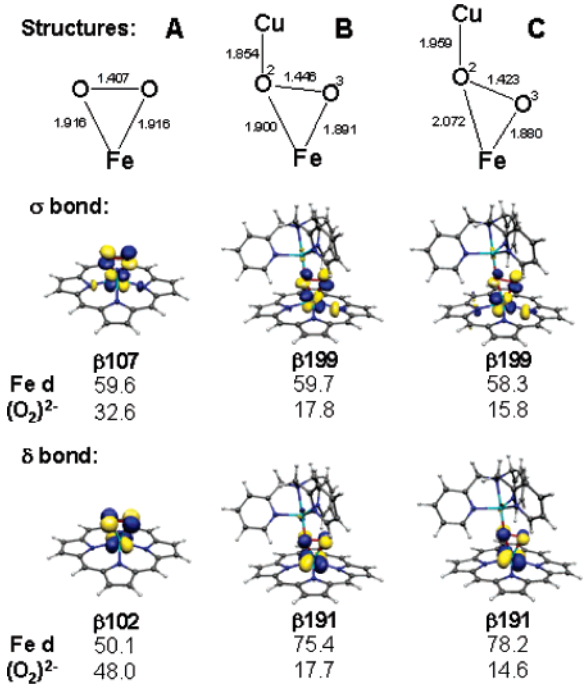

Figure 9. Schematic representation and selected distances and orbitals of $[(P)Fe^{III}-(O_2^{2-})]^-$ (A), 3.7 Å Fe···Cu constrained $[(P)Fe^{III}-(O_2^{2-})-Cu^{II}(TMPA)]^+$ (B), and fully optimized $[(P)Fe^{III}-(O_2^{2-})-Cu^{II}(TMPA)]^+$ (C).

and antibonding orbitals (4.2 eV) compared with the 1.2 eV splitting between the bonding and antibonding orbitals of the δ interaction.

Note that the d orbitals of the $[(P)Fe^{III}-(O_2^{2-})]^-$ complex display an unusual energy level ordering: $d_{xy} < d_{yz} < d_{z^2} < d_{x^2-y^2} < d_{xz}$, where the highest energy d orbital is not the $d_{x^2-y^2}$ but the $d_{xz}-\pi^*_\sigma$ hybrid. This is a consequence of two factors: (i) the large out-of-plane displacement of the Fe^{III} atom (0.624 Å) from the porphyrin, which lowers the energy of the $d_{x^2-y^2}$ orbital, and (ii) the strong Fe $d_{xz}-\pi^*_\sigma$ interaction, which raises the energy of the corresponding antibonding molecular orbital. This geometric and electronic structure description accounts for the high degree of rhombicity observed experimentally by EPR for $[(OEP)Fe^{III}-(O_2^{2-})]^-$ (OEP = octaethylporphyrinate).[66] This was also observed for the related $[(P)Mn^{III}-(O_2^{2-})]^-$ complex.[74]

(ii) $[(P)Fe^{III}-(O_2^{2-})-Cu^{II}(TMPA)]^+$. The Fe^{III}−peroxide bond for $[(P)Fe^{III}-(O_2^{2-})-Cu^{II}(TMPA)]^+$ is very similar to that presented above for the $[(P)Fe^{III}-O_2]^-$ complex. A comparison of the constrained $[(P)Fe^{III}-(O_2^{2-})-Cu^{II}(TMPA)]^+$ structure (3.7 Å Fe···Cu) and $[(P)Fe^{III}-O_2]^-$ is considered first because of the similarity in the Fe−O distances (compared to the fully optimized structure) leading to a more symmetric $Fe^{III}-\eta^2$-O_2^{2-} structure (see Figure 9).

As in the case of the $[(P)Fe^{III}-(O_2^{2-})]^-$ complex, the two main bonding interactions between the Fe^{III} and peroxide in the constrained $[(P)Fe^{III}-(O_2^{2-})-Cu^{II}(TMPA)]^+$ (Fe···Cu 3.7 Å) structure arise from the mixing of the Fe d_{xz} with the peroxide π^*_σ and Fe d_{xy} with the peroxide π^*_v, which lead to σ and δ bonds, respectively. The unoccupied MO β-191, associated with the δ bond (see Figure S8, Supporting Information, for this and other selected orbitals of the constrained $[(P)Fe^{III}-(O_2^{2-})-Cu^{II}(TMPA)]^+$ (Fe···Cu 3.7 Å) complex), has a total 75.2% Fe d character (mainly d_{xy}) and 17.7% π^*_v (see Table 3 for details). The σ bond (β-199) has a total 59.7% Fe d character (mainly d_{xz}) and 21.2% π^*_σ. However, due to the presence of the Cu center interacting with one of the oxygen atoms, the orbitals of the peroxide moiety become somewhat polarized, with different mixing coefficients of the two oxygen atoms. For the δ interaction the coefficients are still quite similar, 8.6% (O2) and 9.1% (O3). However, in the case of the σ bond, the coefficients on the O2 and O3 atoms are 9.0% and 12.1%, respectively. Some of the σ interaction with the O2 atom (3.5%) is also localized in the β-193 orbital (mainly Fe d_{z^2}, 58.9%, but with a significant (14%) contribution from the Fed$_{xz}$ orbital; Table S4 and Figure S8).

The description of the Fe^{III}−peroxide bond for the fully optimized $[(P)Fe^{III}-(O_2^{2-})-Cu^{II}(TMPA)]^+$ structure is similar to the one presented for the 3.7 Å Fe···Cu constrained complex, with differences arising from the larger polarization of the O−O bond due to the difference between the Fe−O2 and Fe−O3 distances along with the interaction of the Cu center with one of the oxygen atoms (Figure 9C). The main interactions are still a combination of σ and δ bonds, but now a larger degree of polarization distributes these interactions among several orbitals. The σ interaction (β-199, shown in Figure 6) is mainly localized on the O3 atom (11.8% O3 p_z orbital vs 4.0% O2 p_z orbital). As in the case of the 3.7 Å Fe···Cu constrained complex, some of the σ interaction with the O2 atom (6.2% O2 p_z) is mixed into the β-193 orbital (mainly d_{z^2}, 62.5%, but with a significant (9.0%) contribution from the d_{xz} orbital). The δ interaction is also distributed between two orbitals: (i) β-191 (see Figure 6), with a total 78% Fe d character (mainly d_{xy}; see Table 3) and 14.6% peroxide π^*_v (8.5% O2 p_z orbital and 6.1% O3 p_z orbital), and (ii) β-192 (Figure 6), with 70% Fe d character (mainly d_{yz}, 64.1%, but with 5% d_{xy}) and 10% π_v character, strongly localized (9.6% O3 p_z) on the O3 atom. The latter can be considered as a π interaction between the Fe and O3 (β-192 in Figure 6).

The unusual energy level ordering of the Fe d orbitals for $[(P)Fe^{III}-(O_2^{2-})]^-$ is no longer observed for $[(P)Fe^{III}-(O_2^{2-})-Cu^{II}(TMPA)]^+$. This is due to (i) the smaller displacement of the Fe^{III} center out of the porphyrin plane (0.534 Å vs 0.624 Å for $[(P)Fe^{III}\text{-}O_2]^-$), which raises the energy of the $d_{x^2-y^2}$ orbital, and (ii) the more limited interaction of the peroxide π^*_σ orbital with the Fe d_{xz} (17% vs 33% π^*_σ character for $[(P)Fe^{III}-O_2]^-$). The smaller mixing coefficient of the peroxide in the spin-down antibonding orbitals of the $[(P)Fe^{III}-(O_2^{2-})-Cu^{II}(TMPA)]^+$ complex, as compared with those of $[(P)Fe^{III}-O_2]^-$, indicates a weaker Fe−peroxide bond in the former, due to the bridging interaction with the $[Cu^{II}(TMPA)]^+$ moiety, and is reflected in a longer Fe−peroxide distance: 1.846 Å for $[(P)Fe^{III}-(O_2^{2-})-Cu^{II}(TMPA)]^+$ vs 1.783 Å for $[(P)Fe^{III}-(O_2^{2-})]^-$ (distance from the Fe to the center of the O−O bond).

4. Discussion

The Fe···Cu distance, obtained from Cu and Fe K-edge EXAFS spectroscopy in both solution and solid state, of the untethered complex $[(F_8TPP)Fe^{III}-(O_2^{2-})-Cu^{II}(TMPA)]^+$ (**1**) is 3.72 Å. This distance is ~0.2 Å shorter than that observed by X-ray crystallography in a tethered complex, $[(TMP)Fe^{III}-(O_2^{2-})-(5MeTPA)Cu^{II}]^+$ (**2**).[29] Recently, EXAFS data for a similar tethered complex, $[(^6L)Fe^{III}-(O_2^{2-})-Cu^{II}][B(C_6F_5)_4]$ (**L6**),[30,36] were reported with an Fe···Cu distance of 3.4 Å. Here, Cu and Fe K-edge EXAFS data for **L6** have been remeasured and analyzed. The best fit to the data resulted in an Fe···Cu

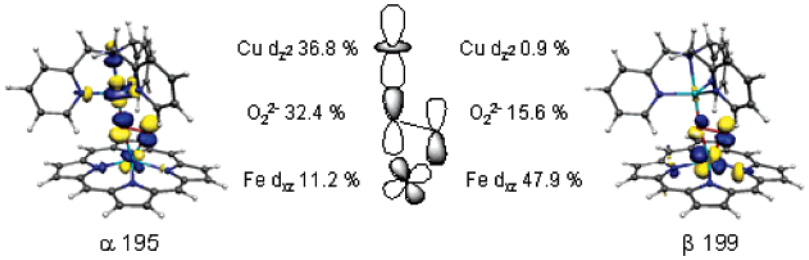

Figure 10. Spin-up unoccupied MO α-195 (LUMO) of the fully optimized model complex $[(P)Fe^{III}-(O_2^{2-})-Cu^{II}(TMPA)]^+$ and a schematic representation of its major contributions, showing the strong antiferromagnetic interaction between the Fe^{III} and Cu^{II} centers.

distance of 3.97 Å (Figures S5 and S6), comparable to the Fe···Cu distance of **2** and that obtained from DFT calculations.[77] Although the ligand architectures of the three complexes are very similar, with a tetradentate TMPA chelate on the copper, a heme group with no axial ligand, and an overall μ-η^1:η^2 peroxide coordination mode, there are some structural and electronic changes between these complexes that could explain their limited structural differences.

The difference of ~0.2 Å in the Fe···Cu distance of **1** as compared to **2** could reflect a combination of steric and electronic factors. For **2**, the steric interaction between the 5-Me-substituted TMPA ligand and the methyl groups of the mesityl substituents of the porphyrin is larger than the interaction between the unsubstituted TMPA ligand and the fluorine atoms of the 2,6-difluorophenyl substituent of the porphyrin in **1**. Also, the reduced donating ability of the 2,6-difluorophenyl substituents of the porphyrin in **1**, compared with that of the mesityl substituents in **2**, could decrease the electron density on the porphyrin ring and allow the Fe and Cu centers a closer approach. The structural differences between **L6** and **1** are much smaller, as the substituents on the porphyrin ring are the same and there is no substituent on the TMPA ligand. The single difference between the two structures is the presence of a tether that links the porphyrin and one of the pyridine rings of the TMPA. The presence of the tether might contribute to the ~0.2 Å longer Fe···Cu distance found in **L6**.

These small structural differences are reflected in the O−O stretching frequencies of these complexes. **2** and **L6** have an O−O stretching frequency of 790 and 788 cm^{-1}, respectively, while the stretching frequency of **1** is shifted up in energy by ~20 cm^{-1} to 808 cm^{-1}. The shorter Fe···Cu distance of **1** results in shorter Fe−O bond distances and stronger Fe−peroxide bonds. As the bonding between the Fe and peroxide involves donation from the π^*_σ and π^*_v peroxide orbitals on the metal, it results in a stronger O−O bond.

To obtain a better understanding of the Fe^{III}−peroxide bonding in $[(P)Fe^{III}-(O_2^{2-})-Cu^{II}(TMPA)]^+$, we have also studied the $[(P)Fe-(O_2^{2-})]^-$ complex. We then include the effects of the $[Cu^{II}(TMPA)]^+$ moiety in $[(P)Fe^{III}-(O_2^{2-})-Cu^{II}(TMPA)]^+$ as a perturbation on the Fe^{III}−peroxide bond in $[(P)Fe-(O_2^{2-})]^-$. Figure 9 shows a schematic representation of the different structures as well as the orbitals associated with the major interactions. The main bonding interaction between the side-on peroxide and the high-spin Fe^{III} center in $[(P)Fe-(O_2^{2-})]^-$ involves the π^*_σ molecular orbital of the O_2^{2-} (in the Fe−O_2 (*xz*) plane) and the d_{xz} orbital on the iron, giving rise to a strong σ interaction. In addition, and in contrast to the η^2-peroxide non-heme iron complex $[Fe^{III}(EDTA)-(O_2^{2-})]^{3-}$,[76] there is also a δ bonding interaction involving the peroxide π^*_v orbital, perpendicular to the Fe−O_2 plane. The strength of the σ interaction, which raises the energy of the corresponding antibonding Fe d_{xz}−π^*_σ molecular orbital, and the displacement of the Fe atom out of the plane of the porphyrin, which lowers the energy of the $d_{x^2-y^2}$ orbital, are responsible for the unusual energy level ordering for the Fe d orbitals, $d_{xy} < d_{yz} < d_{z^2} < d_{x^2-y^2} < d_{xz}$, calculated for this complex and its observed rhombicity.

In the 3.7 Å Fe···Cu constrained $[(P)Fe^{III}-(O_2^{2-})-Cu^{II}-(TMPA)]^+$ complex, where the two Fe−O distances are very similar, the two main bonding interactions again reflect the mixing of the Fe d_{xz} and d_{xy} orbitals with the π^*_σ and π^*_v of the peroxide, giving rise to σ and δ bonds, respectively. The interaction of the Cu center with one of the oxygen atoms induces some polarization of the O−O bond, resulting in somewhat different coefficients on the two oxygen atoms.

In the fully optimized structure, the perturbation introduced by the $[Cu^{II}(TMPA)]^+$ moiety is larger. In this case, the two Fe−O distances are different (Figure 9) and the O−O bond becomes much more polarized. The two main bonding interactions are still σ and δ, arising from the mixing of the Fe d_{xz} and d_{xy} orbitals with the peroxide π^*_σ and π^*_v, but due to the polarization of the O−O bond, they are distributed among several different orbitals. From Figure 6, the σ interaction with O3 is localized mainly in the β-199 orbital, while the interaction with O2 is distributed between the β-199 and β-193 orbitals. The δ interaction is also distributed between two levels, β-191 and β-192. The former is fairly delocalized between the two oxygen atoms, but the latter is almost completely localized on the O3 atom and can be described as a π bond between the Fe and O3. From the composition of the MOs in Table 3, the amounts of σ and δ bonding between the Fe and each O atom are very similar. However, the additional π interaction is localized on the O3 center and is responsible for the shorter Fe−O3 bond (1.880 Å) as compared with Fe−O2 (2.072 Å).

The σ bonding interaction between the Cu d_{z^2} orbital and the peroxo in-plane π^*_σ is the dominant contribution to the Cu−peroxide bond in $[(P)Fe^{III}-(O_2^{2-})-Cu^{II}(TMPA)]^+$. The bonding is similar, although slightly weaker, to that described previously for $[Cu^{II}_2(TMPA)_2(O_2^{2-})]^{2+}$ due to the stronger interaction of the peroxide with Fe^{III} as compared to that with Cu^{II}.[41]

The significant participation of the Fe d_{xz} orbital (11.2%) in the copper-based α-LUMO (α-195 in Figure 10) is responsible for the strong antiferromagnetic interaction between the high-spin Fe^{III} ($S = {}^5/_2$) and the Cu^{II} ($S = {}^1/_2$) center observed

(77) The EXAFS data of **L6** are different from previously reported data.[36] The reported Fe···Cu of 3.4 Å has been reevaluated in this study, and the EXAFS data are fit with an Fe···Cu and Cu···Fe component of ~3.97 Å. This difference is likely due to differences in sample preparation, as the EXAFS data in **L6** are clearly different from those reported herein.

experimentally.[33,41] The bridging μ-η^1:η^2 peroxide provides a strong σ superexchange pathway (the π^*_σ orbital) between the Cu d_{z^2} and the high-spin Fe^{III} d_{xz} for the antiferromagetic coupling. Figure 10 gives the contour diagram of the MO α-195 and a schematic representation of its major contributions. The corresponding σ superexchange pathway for the spin-down electron is localized mainly on β-199 (Figure 10).[78]

The study of the oxygen reactivity of heme−copper assemblies is of importance in understanding O_2 activation in C*c*O. Although the observed Fe···Cu distance in the C*c*O enzyme (ranging between 4.4 and 5.3 Å) seems too long for the formation of a discreet Fe−peroxide−Cu species, and the previously speculated peroxide intermediate (designated as **P**) in the catalytic cycle actually corresponds to a species where the O−O bond has been cleaved, the presence of (hydro)-peroxide metal-bridged or associated Fe^{III}−OO(H)···Cu_B transients has been speculated on the basis of structural, spectroscopic, and theoretical considerations.[10,22,23] The present study of the geometric and electronic structure of $[(F_8TPP)Fe^{III}-(O_2^{2-})-Cu^{II}(TMPA)](ClO_4)$ is a key starting point in understanding the activation and cleavage of the O−O bond in the protein. The structural differences between this model and the protein include the presence of an axial ligand on the heme in C*c*O, the tyrosine residue covalently bound to a Cu−histidine ligand (which may donate $H^\bullet$ in the catalytic cycle, see Figure 2), and the coordination environment on the copper center, which will dictate differences in the electronic structure of the $Fe^{III}-O_2^{2-}-Cu^{II}$ center that can affect reactivity. The description of the nature of the $Fe^{III}-O_2^{2-}-Cu^{II}$ bonds emphasizes the contribution of the μ-η^1:η^2 peroxide bridging mode to the electronic structure of these complexes and provides a reference for studying the effects of differences in structure and bonding on the physical properties and reactivity of related systems.

(78) Some contribution to the σ superexchange pathway is also present in β-193.

Acknowledgment. This work was supported by NIH DK31450 (E.I.S.), NIH RR-01209 (K.O.H), and GM-60353 (K.D.K). SSRL operations are funded by the U.S. Department of Energy, Office of Basic Energy Sciences. The SSRL Structural Molecular Biology program is supported by the National Institutes of Health, National Center for Research Resources, Biomedical Technology Program, and U.S. Department of Energy, Office of Biological and Environmental Research. D.R. thanks the sixth framework program of the UE for a MC-OIF fellowship. We thank Dr. B. Mondal (Karlin group) for preparation of the **L6** sample.

Supporting Information Available: Preparation of samples, EXAFS data, and Fourier transforms of **1** and **L6** in solution and the corresponding fit parameters; comparison of EXAFS data and Fourier transforms of **1** in solid and solution; structural parameters, molecular orbital contour plots, and energy level diagram of **1** with a Cu···Fe distance constrained at 3.7 Å and of $[(P)Fe^{III}-(O_2^{2-})]^-$ obtained from DFT calculations; and results of DFT calculations performed in Jaguar. This material is available free of charge via the Internet at http://pubs.acs.org.

JA043374R